

ERRATA

Hydrology: A Science for Engineers

B. Hingray, C. Picouet, A. Musy

Published by CRC Press, Taylor & Francis Group, 2014

Due to a technical problem, most figures in Chapter 4
were printed in their French versions. We apologize
for this error.

The corresponding English versions of the figures in
question, Figs. 4.1, 4.2, 4.3, 4.4, 4.5, 4.6, 4.7, 4.8, 4.9, 4.10,
4.12, 4.13, 4.14, 4.15, 4.17 and 4.19 are provided in the
following pages.

The figure captions have been included for the sake of
clarity.

These figures are also available in English on the
following website:

<http://www.lthe.fr/PagePerso/hingray/PDF/ERRATA.pdf>

Fig. 4.1, p. 122

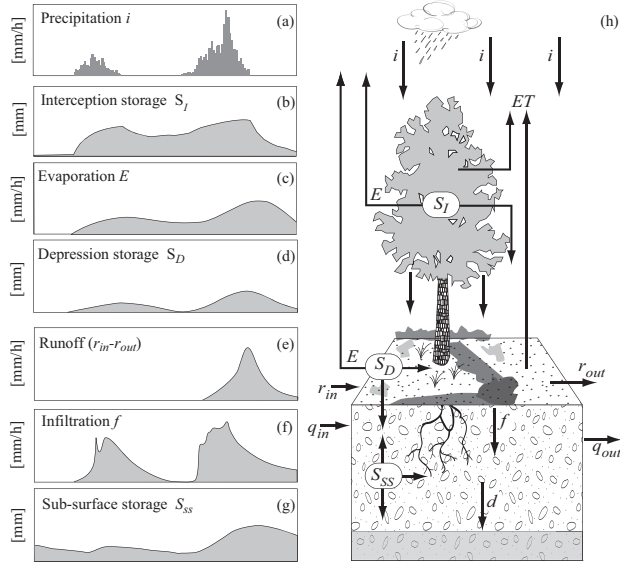


Fig. 4.1: Some of the terms of the water balance equation at the soil-vegetation-atmosphere interface versus time. a) Total rainfall. b) Water stored in the vegetal cover by interception. c) Losses from the vegetal cover by evaporation. d) Water stored in surface depressions. e) Runoff corresponding to the net rainfall (or rainfall excess) on the considered unit area. f) Infiltration. g) Water stored in the unsaturated zone. h) Schematic representation of the different components of the water balance at the scale of a parcel of land.

Fig. 4.2, p. 126

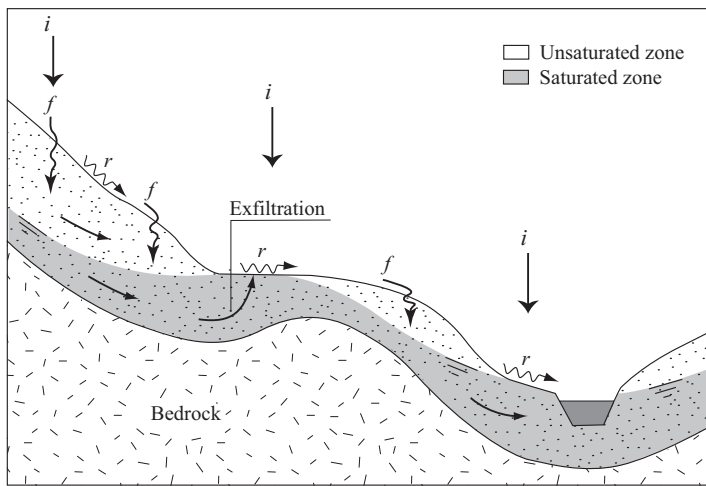


Fig. 4.2: Example of the spatial configuration of the different processes leading to the production of surface runoff in a drainage basin. At the top of the basin, runoff is produced by infiltration excess (Hortonian overland flow) followed by re-infiltration. In the middle of the basin, runoff is produced on saturated surfaces with exfiltration of sub-surface runoff followed by re-infiltration (non-contributing active saturated zones). At the bottom of the drainage basin, runoff is produced on contributing active saturated surfaces (Hewlettian processes) and accompanied by active sub-surface runoff (modified from Cosandey and Robinson, 2000).

Fig. 4.3, p. 127

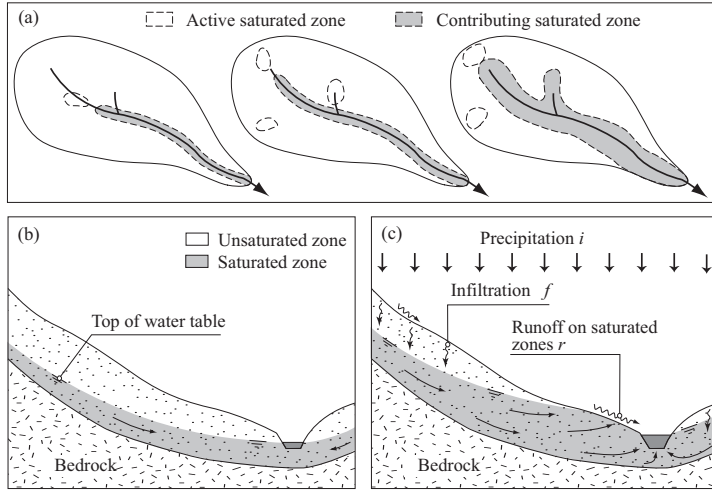


Fig. 4.3: Typical extension of contributing saturated zones during a rainfall-runoff event. a) Plan view of the drainage basin. b) and c) Cross-sectional views.

Fig. 4.4, p. 132

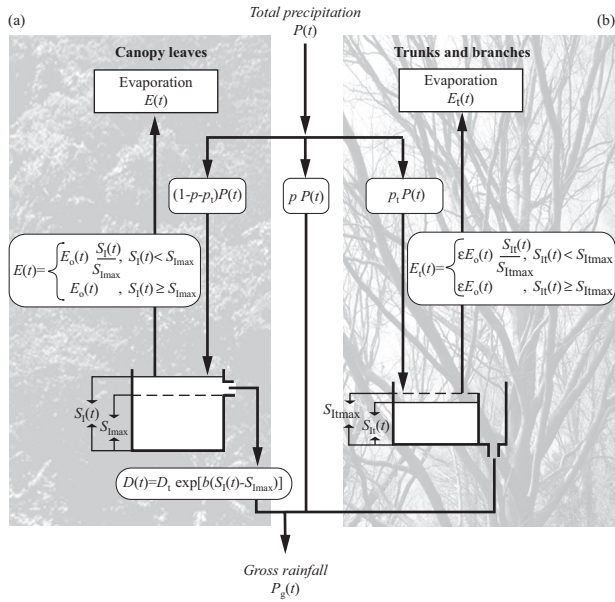


Fig. 4.4: Structure of the Rutter interception model (adapted from Gash and Morton, 1978). The model is a reservoir-based conceptual model. It distinguishes between interception processes on the leaves of the canopy and on the branches and trunks. The reservoirs used to monitor the storage volumes in each of these components each have a maximum storage capacity. The quantity of water $S_\mu(t)$ stored in each reservoir can evaporate at a rate $E_\mu(t)$ (less than or equal to the evaporative capacity $E_0(t)$ or $\varepsilon E_0(t)$, depending on the component) or be drained towards the ground (at rate $D_\mu(t)$ for the canopy) (see Appendix 4.8.1 for a detailed description of the variables and parameters involved).

Fig. 4.5, p. 133

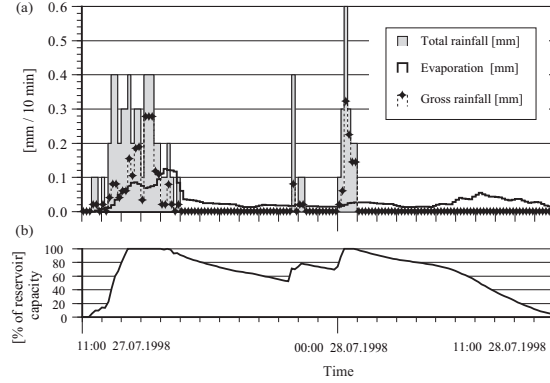


Fig. 4.5: Simulation of the interception process by the Rutter model for a fictitious vegetal cover with parameters $p = p_i = 0.2$; $S_{i\max} = 1.2 \text{ mm}$; $S_{l\max} = 0.8 \text{ mm}$ (see Appendix 4.8.1 for definitions of these parameters). a) Total rainfall (above the canopy), gross rainfall (on the ground) and quantity of water evaporated. b) Variations of storage in vegetal cover (in % of maximum storage capacity).

Fig. 4.6, p. 137

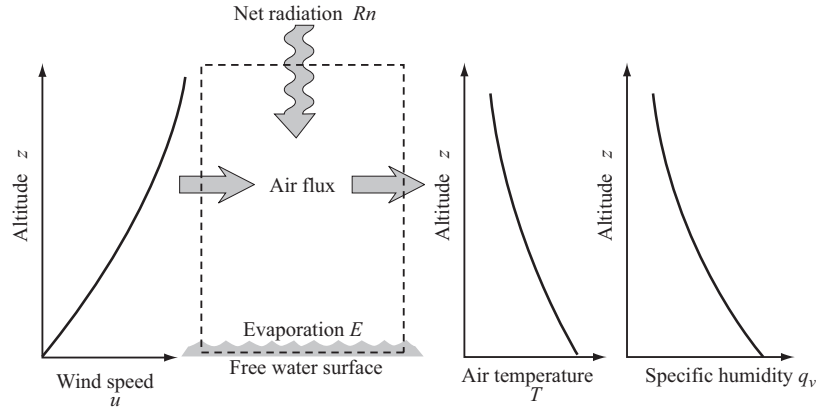


Fig. 4.6: Main mechanisms and explanatory variables determining evaporation fluxes at the SVA interface (adapted from Chow *et al.*, 1988).

Fig. 4.7, p. 140

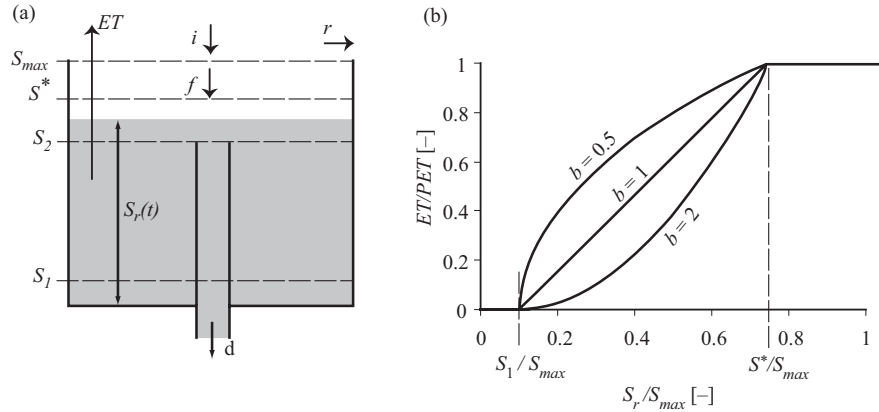


Fig. 4.7: A conceptual root zone reservoir used to estimate the actual evapotranspiration flux related to the presence of the vegetal cover. a) Typical reservoir structure, incoming flux (infiltration, i) and outgoing fluxes (evapotranspiration ET , percolation d and sub-surface runoff r). b) Typical functional relationship between the saturation level of the root zone reservoir and the degree of satisfaction of the evaporative demand.

Fig. 4.8, p. 141

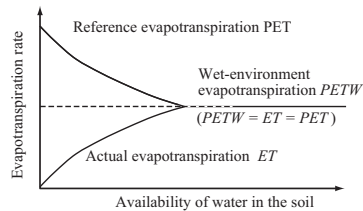


Fig. 4.8: Illustration of the complementary relationship between PET and ET (adapted from Bouchet, 1963).

Fig. 4.9, p. 144

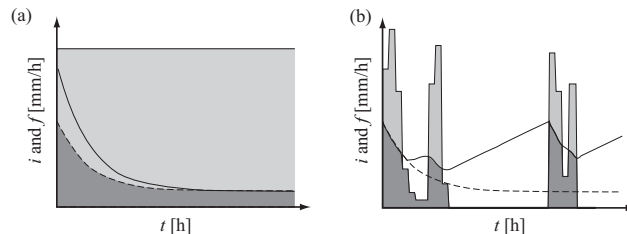


Fig. 4.9: Intensity of gross rainfall (i) and soil infiltration rate (f) for different rainfall events and initial soil saturation conditions. a) Hypothetical case in which the water supply rate is always greater than the infiltration capacity for an initially dry well-drained soil (solid curve) and an initially wet soil (broken curve). b) Infiltration rate (dark gray zone) and infiltration capacity with recovery (solid curve) when the supply rate is alternately less than and greater than the infiltration capacity and infiltration capacity for a supply rate that is always greater than the infiltration capacity (broken line).

Fig. 4.10, p. 145

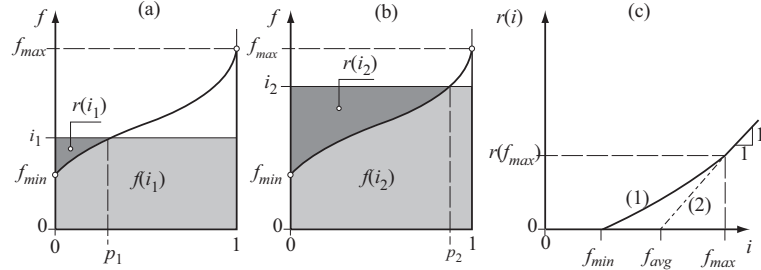


Fig. 4.10: Effect of the spatial variability of infiltration capacity on rainfall excess and infiltration losses at the drainage basin scale when the processes leading to rainfall excess are exclusively Hortonian. Runoff (dark gray zones) and total infiltration (light gray zones) at a given time for gross rainfall intensities: a) i_1 and b) $i_2 > i_1$. The resulting curves represent the statistical distribution function of the soil infiltration capacity for the drainage basin at a given time (infiltration capacity f not exceeded for a fraction c of the total basin area). The potential maximum infiltration rate at the considered time corresponds to the integral under the curve. c) Runoff volumes at the basin scale as a function of gross rainfall intensity considering: (1) the variability of local infiltration capacities and (2) only the average value of the corresponding distribution.

Fig. 4.12, p. 151

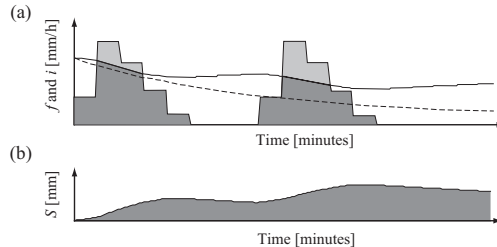


Fig. 4.12: Simulation of infiltration with an IEM type reservoir model where $f_{max}(S) = f_o - cS$. a) Hyetographs of gross and infiltrated rainfall, simulated potential infiltration capacity (solid curve) with the IEM and infiltration capacity according to the Horton model $f(t) = f_c + (f_o - f_c)e^{-ct}$ (dotted curve). b) Change of storage in the soil reservoir S with time.

Fig. 4.13, p. 154

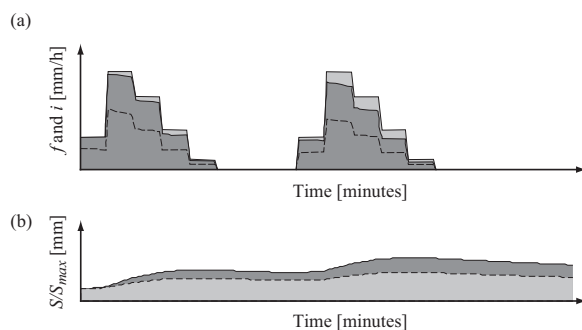


Fig. 4.13: Simulation of infiltration by a global reservoir model with $f(S) = (1 - (S/S_{max})^a) \cdot i_b(t)$ and $Q(S) = S/K$ ($K = 5$ h; $S(t_0) = 20$ mm; $S_{max} = 160$ mm). a) Hyetographs of gross rainfall and infiltrated rainfall obtained for $a = 0.5$ (gray curve) and $a = 2$ (broken curve). b) Storage in the soil reservoir S versus time for $a = 0.5$ (gray curve) and $a = 2$ (broken curve).

Fig. 4.14, p. 155

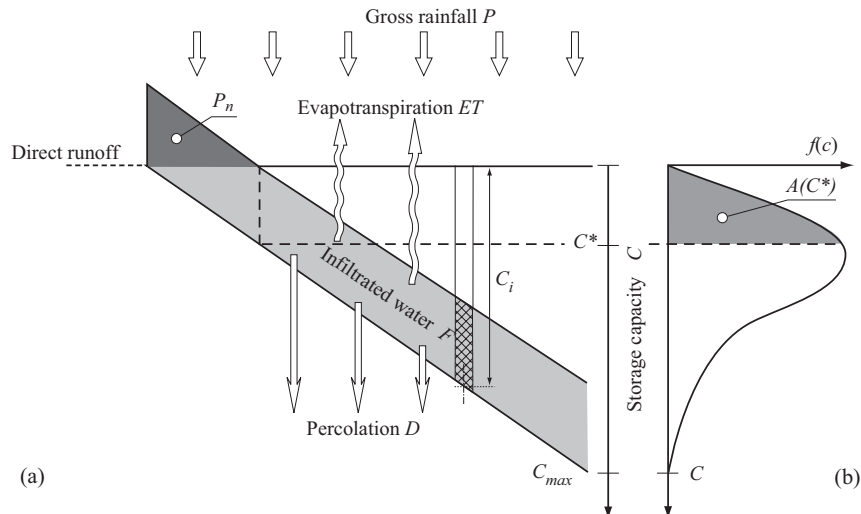


Fig. 4.14: Principle of estimation of infiltration by the Probability Distributed Model (PDM) of Moore and Clarke (1981). a) Storage elements with insufficient storage capacity to absorb the gross rainfall (dark gray area). These elements determine the net rainfall and the fraction of saturated areas. b) The distribution function used to describe the spatial variability of storage capacity over the basin.

Fig. 4.15, p. 156

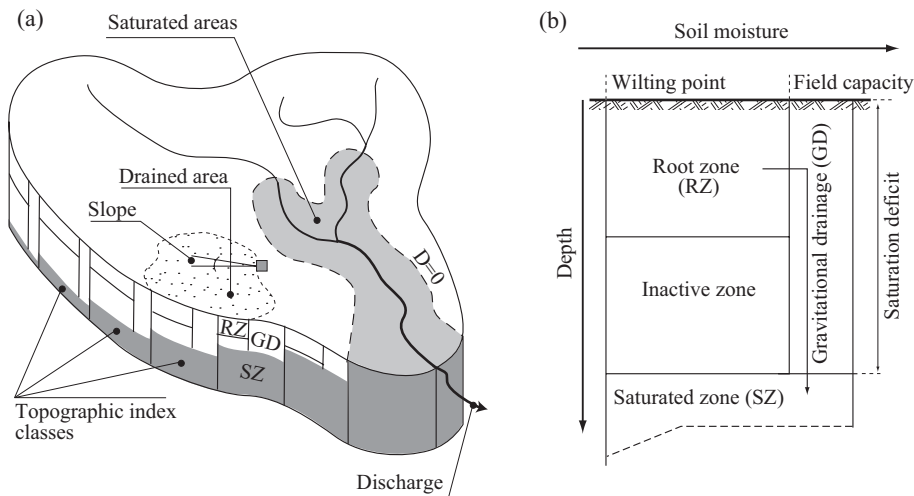


Fig. 4.15: Rainfall excess concept for the Topmodel distributed model (Beven *et al.*, 1984). a) The characteristics used to locally define the value of the topographic index, topographic index classes and saturated areas of the basin at a given time (areas defined by the parts of the basin where the value of the index implies a zero soil saturation deficit at the considered time). b) Schematic representation of the model used to simulate the behavior of each topographic index class.

Fig. 4.17, p. 160

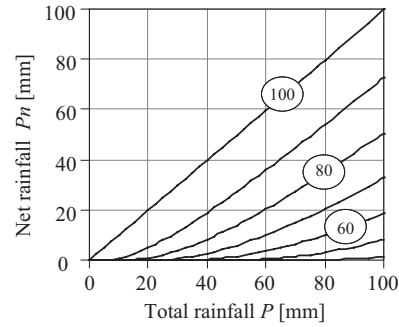


Fig. 4.17: Net rainfall depths obtained using the SCS-CN method versus total rainfall depths for different values of CN.

Fig. 4.19, p. 163

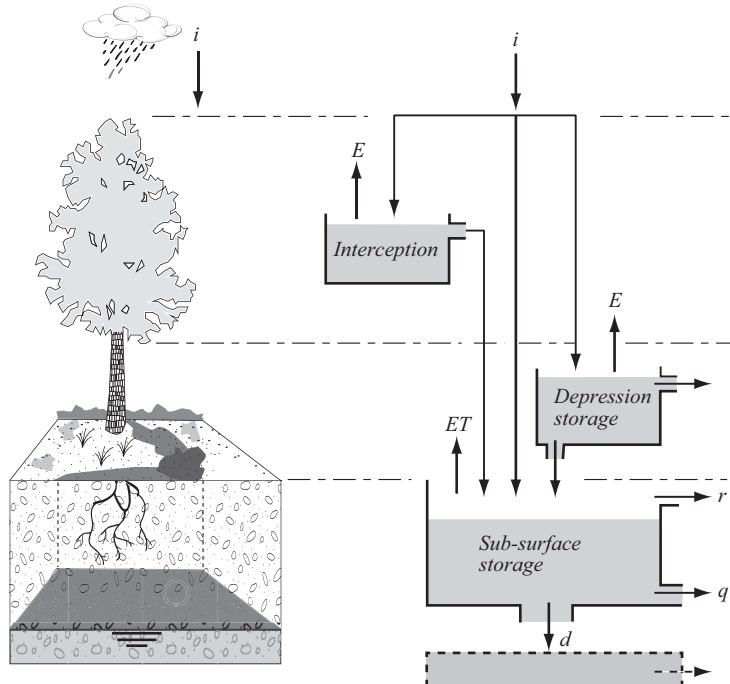


Fig. 4.19: Possible structure of the rainfall excess module of a hydrological model of a drainage basin.